ACS APPLIED MATERIALS & INTERFACES

Research Article

www.acsami.org

Tin–Germanium Alloys as Anode Materials for Sodium-Ion Batteries

Paul R. Abel,[†] Meredith G. Fields,[†] Adam Heller,[†,§] and C. Buddie Mullins*[,†,‡,§,⊥]

[†]McKetta Department of Chemical Engineering, [‡]Department of Chemistry, [§]Center for Electrochemistry, and [⊥]Texas Materials Institute and Center for Nano- and Molecular Science, University of Texas at Austin, 1 University Station, C0400, Austin, Texas 78712-0231, United States

Supporting Information

ABSTRACT: The sodium electrochemistry of evaporatively deposited tin, germanium, and alloys of the two elements is reported. Limiting the sodium stripping voltage window to 0.75 V versus Na/Na+ improves the stability of the tin and tin-rich compositions on repeated sodiation/desodiation cycles, whereas the germanium and germanium-rich alloys were stable up to 1.5 V. The stability of the electrodes could be correlated to the surface mobility of the alloy species during deposition suggesting that tin must be effectively immobilized in order to be successfully utilized as a stable electrode. While the stability of the alloys is greatly increased by the presence of germanium, the specific Coulombic capacity of the alloy decreases with increasing germanium content due to the lower Coulombic capacity of germanium. Additionally, the presence of germanium in the alloy suppresses the formation of intermediate phases present in the electrochemical sodiation of tin. Four-point probe resistivity measurements of the different compositions show that electrical resistivity increases with germanium content. Pure germanium is the most resistive yet exhibited the best electrochemical performance at high current densities which indicates that electrical resistivity is not rate limiting for any of the tested compositions.

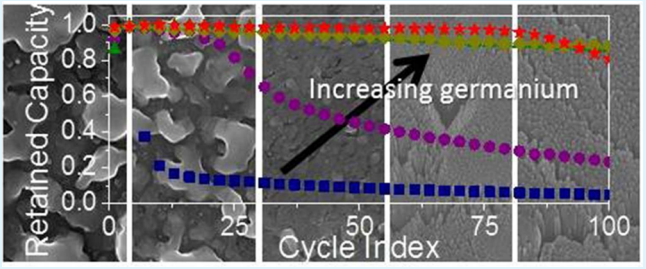

KEYWORDS: *tin, germanium, alloy, sodium-ion battery*

INTRODUCTION

Sodium batteries have the potential for significant cost advantages over lithium batteries and are attractive for stationary applications where cost is a limiting factor. The Na–S and Na–$NiCl_2$ batteries offer such an advantage, but they utilize liquid electrodes, require ceramic electrolytes, and operate at temperatures on the order of 300 °C.[1,2] Their high operating temperature makes them less attractive for intermittent or on-demand applications. Recent identification of new intercalation materials for Na-ion battery cathodes has refreshed the effort to develop Na chemistries that operate at room temperature.[3−12] Many sodium intercalation compounds behave similarly to their lithium analogues;[6,13,14] however, Na ions will typically not intercalate into graphite although other carbon allotropes show a small reversible capacity.[15−17] This has led to a presently ongoing search for safe, abundant, and robust materials for Na-ion battery anodes.

Group IV elements have been well studied as anode materials for lithium-ion batteries.[18−32] In their recent study Chevrier and Ceder calculated the voltages at which the heavier group IV elements alloy with sodium.[15] Experimental data are available for germanium,[33,34] tin,[35−38] and lead.[39] Sodium alloys with Sn up to a thermodynamic limit of $Na_{15}Sn_4$ provide a theoretical capacity of 847 mAh g^{-1}, making it an attractive candidate. However, the capacity is not well retained on cycling, with particle aggregation and electrode/electrolyte instability being cited as causes of degradation.[40−43] While limiting the potential range of cycling improves the stability,[42] operating anode potentials in functioning batteries are rarely well-defined. Additionally, active/inactive matrices,[44,45] composites,[46,47] and alloys have been investigated as methods for stabilizing tin electrodes.[48,49]

The technology of alloying elements to change material properties is nearly as old as civilization itself. The Bronze Age is named after one of the first metallurgical discoveries, the alloying of copper and tin, resulting in a much harder metal. By alloying tin with other elements, physical, chemical, and electrochemical properties can be significantly altered, and by appropriate selection of Sn-alloying element(s), anode materials can be improved. This principle has been demonstrated in the literature with the addition of copper to tin electrodes for sodium-ion batteries. Sn–Cu compounds will have a melting point that is significantly higher than that of pure tin, and as a result, the Sn–Cu alloys are more resistant to agglomeration and electrochemical sintering. As expected, Sn–Cu electrodes with 10 at% copper show significant improvements in stability; however, the specific capacity is decreased by the additional weight of the inactive Cu in the electrode.[48]

Alloying tin with other sodium-active elements is a potential method for improving the electrode stability without sacrificing capacity. Other group IV elements such as Ge have limited solubility in tin at room temperature,[50] but metastable

Received: May 28, 2014
Accepted: August 26, 2014
Published: August 26, 2014

amorphous alloys of tin and germanium have been synthesized for study as semiconductor materials. Vacuum evaporative deposition and sputtering allowed the growth of single-phase, amorphous tin−germanium alloys over a much wider compositional range than allowed by traditional processing techniques.[51,52] Furthermore, such alloys exhibit tetrahedral short-range order as well as random arrangement of their constituent elements. Group IV alloys such as Si−Ge[19] and Sn−Ge[53−55] have been investigated as lithium-ion battery anodes, and Sn−Ge−Sb ternary alloys have recently been investigated for sodium-ion batteries;[56] however, the electrochemical properties of alloy systems are still not well understood.

Here we grow well-defined thin films of Sn−Ge alloys of various compositions by vacuum deposition and test them as sodium-ion battery anodes. Additionally, we use glancing angle deposition (GLAD) for microstructural and porosity control and as a method for measuring the mobility of adatoms during deposition. GLAD is a physical vapor deposition technique in which adatoms impinge on the substrate at a glancing angle (in our case, we use 70° from surface normal). GLAD will produce nanostructured films if the surface diffusion of adatoms is limited.[57] In the early stages of deposition, stochastic variations in the deposition rate tend to roughen the surface. That roughness is amplified by self-shadowing and leads to the growth of porous films.[58] In these films, morphology is controlled by the deposition angle and ranges from dense at angles close to normal, to porous, reticulated, and then nanocolumnar as the deposition angle is increased.[59] If surface diffusion is possible, however, the shadowed regions of the substrate are accessible to the adatoms through diffusional processes, and dense films result independent of deposition angle. Adatom surface diffusion is related to substrate temperature with growth of nonequilibrium structures possible if the substrate temperature is held below approximately 1/3 of the melting point of the deposited material.[60] If the substrate is held at temperatures above this value (as is the case for a room-temperature substrate when depositing tin metal) surface diffusion dominates, and the morphology is controlled by the surface energies of the materials—dense films form if the deposited material wets the substrate, and micron-scale islands form if the deposited material is nonwetting. The ability of the tin−germanium alloys deposited in this study to support nanostructured growth varied with composition, and the electrochemical stability of the alloys was well correlated to their ability to form nanostructures during deposition. Additional details, examples, and applications of GLAD can be found elsewhere.[18,19,61,62]

EXPERIMENTAL SECTION

Material Synthesis. Tin−germanium alloy electrodes were vacuum deposited by coevaporation of tin (Alfa Aesar 99.999%) and germanium (Kurt J. Lesker 99.999%) using electron beam evaporators. The composition of the Sn−Ge alloys was controlled by varying the ratio of the fluxes from the individual evaporators. The deposition rate for each element was independently measured and balanced to grow a film of the desired composition. The base pressure of the chamber was $<1 \times 10^{-7}$ Torr but increased to $\sim 5 \times 10^{-7}$ Torr during deposition. Material for electrochemical testing and SEM imaging was deposited on 15.6 mm diameter stainless steel substrates (Pred Materials) at an incident angle of 0° or 70° from the surface normal, while material for resistivity measurements was deposited on glass slide covers (Fisher Scientific). The substrates were cleaned by sonication in ethanol prior to deposition. The deposition rate of each evaporator was calibrated using a quartz crystal microbalance (QCM) (Inficon SQM-160 with cool-drawer sensor feed-through), and the ratio of deposition rates was used to calculate film composition. The total mass density of each electrode used in this study was 50 $\mu g\ cm^{-2}$.

Material Characterization. SEM images of the electrodes were obtained with a Hitachi S5500 equipped with a Bruker X-ray detector for EDX measurements. XRD was performed on a Philips X-PERT theta−theta diffractometer. Resistivity measurements were made with a Lucas four-point probe employing a Keithley 220 programmable current source. The composition was measured by XPS using a commercial X-ray photoelectron spectrometer (Kratos Axis Ultra), utilizing a monochromatic Al−Kα X-ray source ($h\nu$ = 1486.5 eV). An automated charge neutralizer was employed for analysis. Casa XPS analysis software was used to determine the stoichiometry of samples from corrected peak areas, employing Kratos sensitivity factors for each element of interest.

Electrochemical Testing. As-deposited films were assembled into 2032 coin cells in an argon-filled glovebox (MBraun Unilab) with oxygen and water levels held below 5 ppm. Sodium metal (Sigma-Aldrich, ACS Reagent) was used as the counter/pseudoreference electrode and 1 M $NaPF_6$ (Alfa Aesar, 99+%) in a 1:1 mixture of fluorinated ethylene carbonate (Solvay Chemicals) and diethyl carbonate (Sigma-Aldrich, battery grade) as the electrolyte. Celgard 2400 polypropylene membrane was used as the separator. Cells were galvanically cycled using an Arbin BT2043 multichannel battery tester. Cells were cycled between 5 mV and either 0.75 or 1.5 V versus the Na/Na^+ redox couple. The galvanostatic intermittent titration technique (GITT) was also performed using the BT2043. Cells underwent a conditioning cycle at C/10 prior to GITT testing which consisted of 30 min current pulses at a rate of C/20 followed by 30 min of rest in order for the cells to relax back toward an equilibrium state.

RESULTS AND DISCUSSION

Films with nominal compositions Ge, $Ge_{0.75}Sn_{0.25}$, $Ge_{0.5}Sn_{0.5}$, $Ge_{0.25}Sn_{0.75}$, and Sn were analyzed by XPS in order to verify the final composition of the films. All compositions were deposited at 0° in order to grow dense films. Quantitative analysis of the Ge $2p_{1/2}$ feature at 1248 eV and the Sn $3d_{5/2}$ feature at 485 eV was used to determine the film compositions. These features are shown in Figure 1. Quantitative analysis of the features provided film compositions very close to the nominal values calculated from QCM measured fluxes. The measured values for the intermediate compositions were $Ge_{0.79}Sn_{0.21}$, $Ge_{0.45}Sn_{0.55}$, and $Ge_{0.26}Sn_{0.74}$. For simplicity, we continue to label the films by their nominal compositions. Both the tin and germanium show measurable oxidation, with a germanium oxide peak at 1251 eV and a tin oxide peak at 487 eV. XPS, however, is a surface-sensitive technique, and no precautions were taken to prevent surface oxidation on the samples. We can conclude that the oxide layer is thin based on the strong contribution from elements in their metallic states.

SEM images of Sn−Ge films deposited at 0° as well as 70° are shown in Figure 2. While there is a marked difference in morphology between the films deposited at different angles for pure germanium, the two pure tin films look identical. This is due to the difference in surface mobility between the two species. The substrate is radiatively heated by the evaporators, and tin is much more mobile than germanium at the substrate temperature of ~50 °C during deposition. The substrate temperature is high enough for tin adatoms to migrate into any shadowed regions by surface diffusion when the tin is deposited at a glancing angle. The absolute substrate temperature is roughly 64% of tin's absolute melting point; in comparison, the absolute substrate temperature is only 26% of the absolute melting point of Ge. The deposited alloys are metastable phases not represented on the phase diagram and thus do not have a

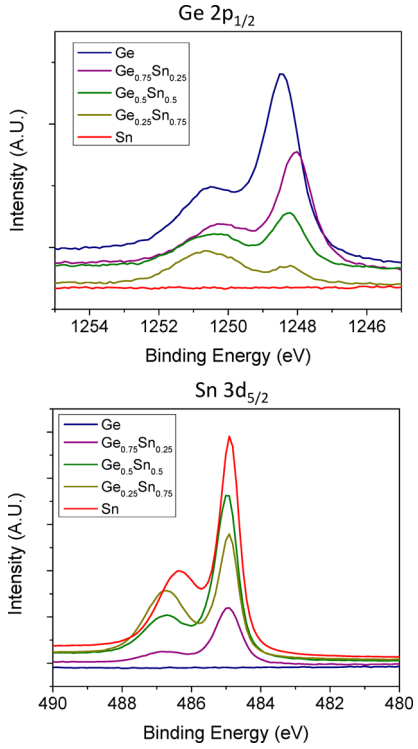

Figure 1. XPS on Sn−Ge alloy electrodes. The Ge $2p_{1/2}$ and Sn $3d_{5/2}$ features are shown. Quantitative analysis was used to determine the elemental composition of each film.

well-defined melting point. The liquid species, however, are completely miscible, and if we use substrate temperature as a fraction of the liquidus as a predictor of stability, we get values of 29%, 31%, and 36% for $Ge_{0.75}Sn_{0.25}$, $Ge_{0.5}Sn_{0.5}$, and $Ge_{0.25}Sn_{0.75}$ respectively. This analysis agrees with the SEM images of films deposited at 70° (Figure 2) where Ge and $Ge_{0.75}Sn_{0.25}$ are nanostructured, while $Ge_{0.25}Sn_{0.75}$ and pure Sn are dense. $Ge_{0.5}Sn_{0.5}$ appears to be a transition case where there is significant porosity in the film, but it is not nanostructured to the degree of the higher germanium content films. The nanostructured films (Ge and $Ge_{0.75}Sn_{0.25}$) had column diameters of ∼10 nm; $Ge_{0.5}Sn_{0.5}$ had a characteristic length scale of ∼200 nm; and the tin-rich films ($Ge_{0.25}Sn_{0.75}$ and Sn) formed domains of 500−800 nm in size. This is consistent with the surface atoms being increasingly mobile as the mole fraction of tin is increased. We therefore expect the films with the highest tin content to be the least stable on cycling. The morphology of the films deposited at 0° also changes with composition. Tin does not wet the stainless steel substrates used in this study and formed isolated islands rather than a conformal film during deposition. The film roughness and prevalence of such islands increased with the film's tin content. On the basis of the SEM images, 0° films were used for all electrochemical testing in order to give films with more similar morphology across the entire compositional range

Figure 3 shows X-ray diffraction patterns for thin films of each composition. The only visible features in the Ge and

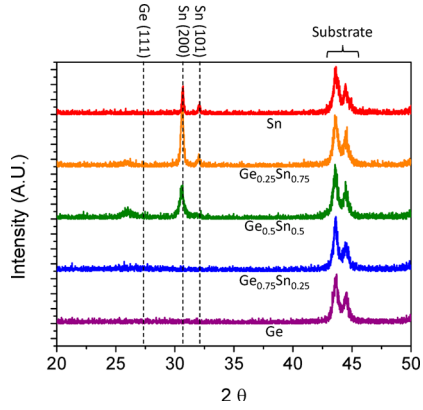

Figure 3. XRD patterns of as-deposited Sn−Ge films of each composition.

$Ge_{0.75}Sn_{0.25}$ films at 43.6° and 44.5° are due to the stainless steel substrate. The high melting point of germanium leads to the deposition of completely amorphous films, and high concentrations of germanium decrease the mobility of tin. Crystalline peaks for β-tin are observed for $Ge_{0.5}Sn_{0.5}$, $Ge_{0.25}Sn_{0.75}$, and pure Sn. This is consistent with the findings of Maruyama and Akagi, who found that crystalline β-tin formed for compositions with more than 38 at% tin.[63] The intensity of the Sn (1 0 1) peak at 32° decreases, while the Sn (2 0 0) peak at 30° broadens and shifts to lower angles with increasing germanium content. This indicates that the tin lattice is increasingly strained as the germanium content of the film is increased. A

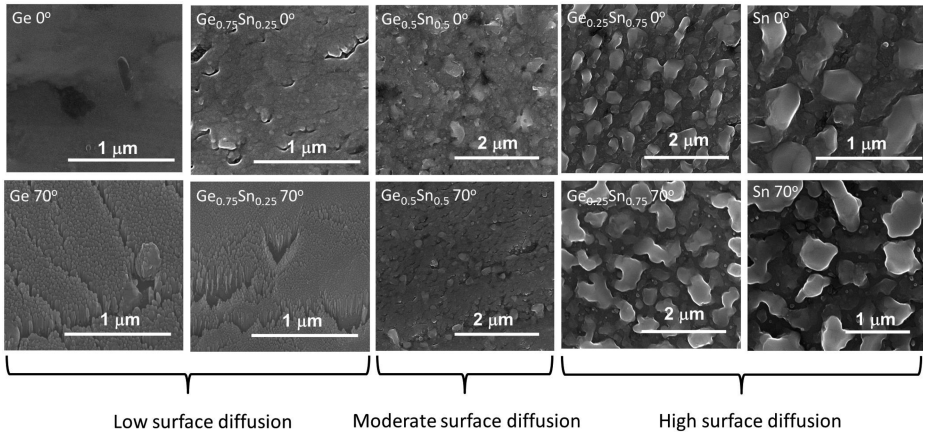

Figure 2. SEM images of Sn−Ge alloy films. Films of each composition are shown deposited at both 0° and 70° from the surface normal. Surface diffusion is qualitatively assessed based on the ability of the 70° films to form nanostructures during deposition.

detailed view of the tin (1 0 1) and (2 0 0) features is shown in Figure S1 in the Supporting Information. A diffuse, low intensity feature near 26° is present in the $Ge_{0.5}Sn_{0.5}$ and $Ge_{0.25}Sn_{0.75}$ films. This feature is likely due to the presence of a diamond cubic alloy phase where tin substitutes into the germanium lattice. Such phases have been previously reported, with the lattice constants increasing with tin content. The diffuse nature and low intensity of the peak indicate that the phase is poorly crystallized.[64,65] This is consistent with the limited adatom surface mobility at this composition. At higher germanium compositions, the mobility of adatoms is decreased so that the deposited films are completely amorphous and this feature is absent. At lower germanium content, the mass fraction of this phase is decreased, thus decreasing the peak intensity.

Thin films of each alloy, deposited at 0° in order to have a more consistent morphology for all samples, were cycled as a constant current C/2 between 5 mV and either 0.75 or 1.5 V in order to investigate the cycling stability of each composition. The cycling results are shown in Figure 4. When cycled up to

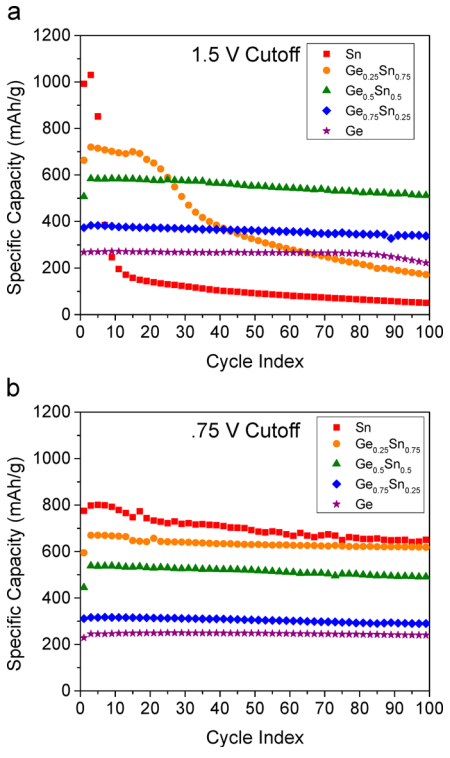

Figure 4. Stability of Sn−Ge alloy films cycled at C/2 between a lower cutoff voltage of 5 mV and an upper cutoff voltage of either (a) 1.5 V or (b) 0.75 V.

1.5 V, the capacity of both the tin and the $Ge_{0.25}Sn_{0.75}$ electrodes degraded rapidly. The tin electrode only survived for four cycles before the capacity dropped significantly, while the $Ge_{0.25}Sn_{0.75}$ survived for ~20 cycles before it began to degrade appreciably. At germanium compositions of 50 at% and higher, however, the capacity remained stable for the full 100 cycles. The stability of the films and the ability of that material to form nonequilibrium structures during deposition follow the same trend; this suggests that the observed electrode degradation is related to the mobility of the electrode material. By increasing the liquidus of the alloy, the mobility of the constituent atoms is decreased, and the stability of the electrode is increased.

If the upper cutoff voltage is reduced from 1.5 to 0.75 V, all compositions remain stable for the duration of the 100 cycle test with the exception of pure tin. While the tin electrode is not perfectly stable, its stability is greatly increased. For the 0.75 V case, the tin electrode retains 83% of its initial capacity after 100 cycles, whereas only 5% is retained when the cutoff voltage is 1.5 V. The decrease in upper cutoff voltage also reduced the reversible capacity of all electrode compositions. This indicates that some sodium remains alloyed with the electrode at the upper cutoff voltage; i.e., the sodium is incompletely stripped from the electrode.

Voltage profiles for the first and second cycles for all of the compositions are shown in Figure 5. Figure 5a shows cycling

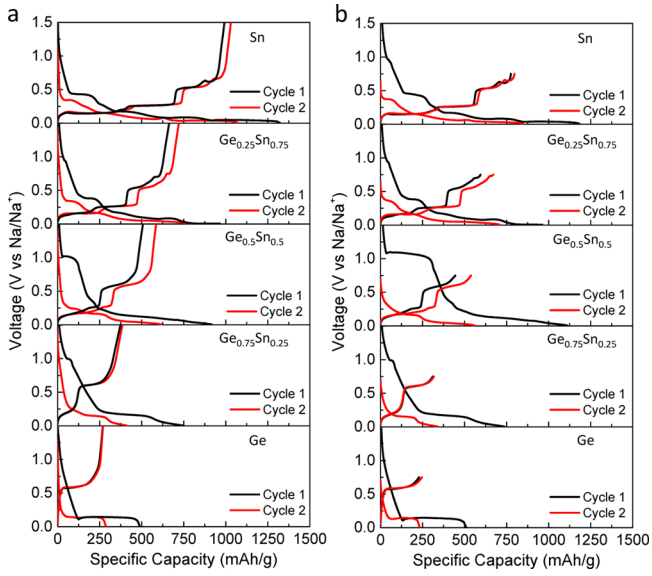

Figure 5. Voltage profiles for the first and second sodiation cycles of tin−germanium alloys at C/2 and with an upper cutoff voltage of (a) 1.5 V and (b) 0.75 V.

between 5 mV and 1.5 V, and cycling to the reduced upper cutoff voltage of 0.75 V is shown in Figure 5b. Regardless of the cutoff voltage, the tin electrode shows voltage plateaus for sodium stripping at 660, 530, 270, 210, and 150 mV. The plateaus at 660, 530, 270, and 150 mV have been indexed by Ellis et al. to the following reactions, respectively[35]

$$3Sn + Na \leftrightarrow NaSn_3 \ (660\ mV) \quad (1)$$

$$1/3NaSn_3 + 2/3Na \leftrightarrow a\text{-}NaSn \ (530\ mV) \quad (2)$$

$$4a\text{-}NaSn + 5Na \leftrightarrow Na_9Sn_4 \ (270\ mV) \quad (3)$$

$$Na_9Sn_4 + 6Na \leftrightarrow Na_{15}Sn_4 \ (150\ mV) \quad (4)$$

Recent work by Baggetto et al. indicates that the reaction mechanism between sodium and tin is more complicated than the model proposed by Ellis et al. with many metastable phases offering alternate reaction pathways.[38] They observed that the desodiation features corresponding to reaction 3 at 270 mV and reaction 4 at 150 mV could be partially or fully replaced by a single desodiation plateau at 200 mV. They postulated that this sodium stripping plateau was the result of the direct conversion of fully sodiated $Na_{15}Sn_4$ to a metastable phase with a

stoichiometry close to $Na_{1.2}Sn$. This reaction is likely responsible for the 210 mV feature present in Figure 5.

Baggetto et al. also reported high voltage desodiation features at 1.4 and 1.9 V.[38] These features were kinetically limited, and the absence of the 1.4 V feature in tin electrodes cycled to 1.5 V is likely due to the higher rates used in this study.

The sodiation of germanium is a much simpler process with only a single sodium insertion plateau at 140 mV and a single extraction plateau at 590 mV. As germanium is added to the tin, the redox potential of the phase transformations are changed, and the formation of certain phases is suppressed. $Ge_{0.25}Sn_{0.75}$ exhibits four sodium stripping plateaus at 750, 540, 260, and 160 mV; $Ge_{0.5}Sn_{0.5}$ exhibits three plateaus at 580, 270, and 170 mV; and $Ge_{0.75}Sn_{0.25}$ exhibits two plateaus at 600 and 210 mV. The voltage for each phase transformation for each composition is shown in Figure 6. When 25 at% germanium

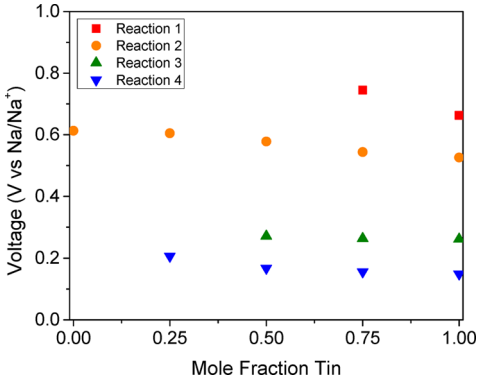

Figure 6. Voltage of sodium extraction plateaus plotted as a function of electrode composition.

is added to tin, the potential for reaction 1 shifts from 660 to 745 mV, and the reaction is completely suppressed in $Ge_{0.5}Sn_{0.5}$ and alloys with higher germanium content. Both tin and germanium form 1:1 alloys with sodium; however, germanium does not form any intermediate phase between Ge and NaGe,[66] explaining the disappearance of a plateau for reaction 1 in germanium-rich alloys, while the plateau for reaction 2 merely shifts from 530 mV for tin, to 550 mV for $Ge_{0.25}Sn_{0.75}$, to 590 mV for $Ge_{0.5}Sn_{0.5}$, and to 610 mV for $Ge_{0.75}Sn_{0.25}$. Reaction 3 does not exhibit significant changes in potential with composition, remaining near 270 mV for all tested compositions; only the magnitude of the plateau changes. The magnitude, however, drops faster than would be expected from the percentage of tin in the alloy. For $Ge_{0.25}Sn_{0.75}$, the capacity of this plateau dropped from 278 mAh/g, for pure tin, to 174 mAh/g, a reduction of 37%, whereas the tin content has only been reduced by 25%. For $Ge_{0.5}Sn_{0.5}$ the magnitude has been reduced to 50 mAh/g, a reduction of 82%. The feature completely disappears in the $Ge_{0.75}Sn_{0.25}$ electrode. The feature for reaction 4 also increases in voltage from 150 mV for pure tin to 160 mV for $Ge_{0.25}Sn_{0.75}$, 170 mV for $Ge_{0.5}Sn_{0.5}$, and 210 mV for $Ge_{0.75}Sn_{0.25}$ and is absent for pure germanium films.

Galvanostatic intermittent titration technique measurements were performed on tin, germanium, and alloy electrodes, and the resulting quasi-equilibrium potential profiles are shown in Figure 7. The sodiation overpotentials are larger than the desodiation overpotentials for all of the compositions. Previously reported GITT measurements on both pure tin and pure germanium electrodes showed this same asymmetry.[34,38] Looking at changes in overpotential with composition, the magnitude of the desodiation overpotentials decreases with increasing tin content up to $Ge_{0.25}Sn_{0.75}$ before increasing for pure tin. Overpotentials can arise from either reaction kinetics or concentration polarization. However, the overpotential minimum occurring at an intermediate composition suggests that the reduction in overpotentials is due to reductions in concentration polarization as increased compositional disorder leads to faster sodium transport. The voltage of the galvanostatic desodiation plateaus increases monotonically with germanium content, whereas the desodiation overpotentials pass through a minimum at intermediate compositions. This leads to the conclusion that changes in the sodium stripping voltage with composition are due to changes in electrode thermodynamics rather than just arising from changes in the electrode kinetics.

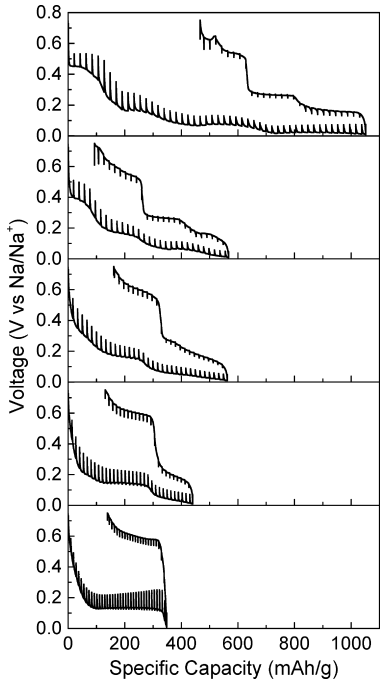

Figure 7. Potential profiles from GITT measurements performed on tin, germanium, and alloy electrodes. GITT measurements were performed after a C/10 conditioning cycle.

C-rate tests were performed on electrodes of each composition. After a conditioning cycle at C/10, each electrode was tested for 10 cycles each at 1C, 2C, 5C, and 10C. The capacity of each composition on the 10th cycle at each C-rate was normalized to the C/10 capacity for that composition, and the normalized capacity as a function of C-rate for each composition is shown in Figure 8. The complete series of C-rate tests is shown in Figure S2 in the Supporting Information, and voltage profiles for each composition at each rate are shown in Figure S3 (Supporting Information). For germanium, the capacity remains nearly constant for rates up to 2C. Above this rate, the capacity drops quickly, with only 50% of the C/10 capacity retained at 10C. The loss in capacity accelerates with increasing C-rate. $Ge_{0.75}Sn_{0.25}$ shows a similar trend; however, the normalized capacity is significantly lower at each C-rate.

Tin shows a different trend as the C-rate is increased. While there is a loss in capacity when the rate is increased from C/10 to 1C, the largest decrease in capacity is between 1C and 2C, and the rate of capacity loss decreases as the C-rate is increased

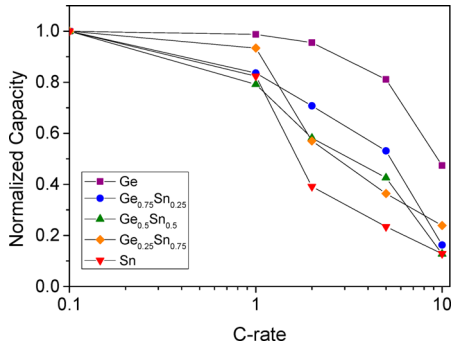

Figure 8. Normalized capacity as a function of C-rate for each composition of the Sn−Ge alloy.

beyond that point. The large drop in capacity between 1C and 2C is partially due to the highest voltage sodium stripping feature being pushed outside the voltage window of the test (see Figure S3 in the Supporting Information). $Ge_{0.25}Sn_{0.75}$ follows the same trend as pure tin, but with an improved normalized capacity at each C-rate.

The stable phase of tin, at room temperature, is metallic β-tin. However, a semimetal, diamond-cubic phase, α-tin, is stable below 13.2 °C. The stable phase of germanium is diamond-cubic, and the amorphous alloys of the two elements were found to have the diamond-cubic short-range order even though they lacked long-range order.[67] The same study found that adding tin to germanium narrows the bandgap of the material, thus increasing the electrical conductivity at room temperature. This trend is reflected in the resistivity measurements shown in Figure 9. The resistivity of the alloy decreases

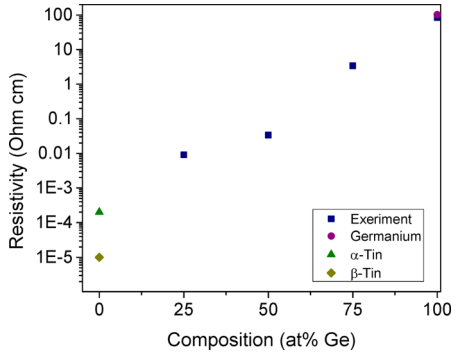

Figure 9. Electrical resistivity measurements for tin−germanium alloys as well as literature values for amorphous germanium,[70] α-tin,[69] and β-tin.

with increasing tin content, from a value of 84 ohm-cm for pure germanium to 9×10^{-3} Ω-cm for $Ge_{0.25}Sn_{0.75}$. We were unable to measure the resistivity of the pure tin film, as tin does not wet the glass substrates that we were using. Instead, the tin formed individual, isolated domains on the surface. As such, the measurements returned the resistivity of the substrate rather than the film. However, the resistivity of tin, as reported in the literature is 1×10^{-5} Ω-cm for the tetragonal β-tin phase[68] and 2.0×10^{-4} Ω-cm for the diamond-cubic α-tin phase.[69]

Because the sodiation reaction is electron mediated, materials with low resistivity are desirable. While pure tin has the lowest resistivity, it is also the least stable composition in this study. The electrodes with high germanium content were much more stable than tin and additionally performed better at high c-rates. This indicates that for all of the compositions studied electrical resistivity was not a limiting factor.

CONCLUSIONS

Tin is a promising sodium-ion battery material, but suffers from poor cycling stability. Tin−germanium alloys deposited by evaporative deposition show improved cycling stability when compared to pure tin. XRD shows that the germanium-rich compositions were completely amorphous, while the tin-rich compositions showed diffraction peaks for crystalline tin and a tin−germanium alloy phase. The ability of a given composition to form nanostructured GLAD films was used as a measure of surface mobility. The addition of germanium to tin raises the liquidus of the melt and reduces the surface mobility of atoms at room temperature. The extent to which the tin atoms were immobilized was well correlated to the cycling stability of the films. This suggests that immobilizing tin is required for it to stably cycle in sodium-ion batteries. Limiting the cycling upper cutoff voltage to 0.75 V also increased the stability of the materials.

ASSOCIATED CONTENT

Supporting Information

Zoomed view of tin (2 0 0) and (1 0 1) X-ray diffraction peak and cycling data and voltage profiles for the C-rate tests for each tested composition. This material is available free of charge via the Internet at http://pubs.acs.org.

AUTHOR INFORMATION

Corresponding Author

*E-mail: mullins@che.utexas.edu.

Notes

The authors declare no competing financial interest.

ACKNOWLEDGMENTS

This work was supported by the Welch Foundation (Grant F-1436 for C.B.M. and F-1131 for A.H.). P.R.A. thanks the Hertz Foundation for a graduate fellowship. M.G.F. thanks the University of Texas Office of the Vice President for Research for an Undergraduate Research Fellowship. The authors thank Solvay Chemicals for providing the fluorinated ethylene carbonate and Celgard for providing the separators used in this study.

ABBREVIATIONS

GLAD, glancing angle deposition; QCM, quartz crystal microbalance; GITT, galvanostatic intermittent titration technique

REFERENCES

(1) Sudworth, J. L. Zebra Batteries. *J. Power Sources* **1994**, *51*, 105−114.

(2) Lu, X.; Xia, G.; Lemmon, J. P.; Yang, Z. Advanced Materials for Sodium-Beta Alumina Batteries: Status, Challenges and Perspectives. *J. Power Sources* **2010**, *195*, 2431−2442.

(3) Lu, Y.; Wang, L.; Cheng, J.; Goodenough, J. B. Prussian Blue: a New Framework of Electrode Materials for Sodium Batteries. *Chem. Commun.* **2012**, *48*, 6544−6546.

(4) Barpanda, P.; Ye, T.; Nishimura, S.-I.; Chung, S.-C.; Yamada, Y.; Okubo, M.; Zhou, H.; Yamada, A. Sodium Iron Pyrophosphate: A Novel 3.0 V Iron-Based Cathode for Sodium-Ion Batteries. *Electrochem. Commun.* **2012**, *24*, 116−119.

(5) Jian, Z.; Zhao, L.; Pan, H.; Hu, Y.-S.; Li, H.; Chen, W.; Chen, L. Carbon Coated $Na_3V_2(PO4)_3$ as Novel Electrode Material for Sodium Ion Batteries. *Electrochem. Commun.* **2012**, *14*, 86−89.
(6) Kim, D.; Lee, E.; Slater, M.; Lu, W.; Rood, S.; Johnson, C. S. Layered $Na[Ni_{1/3}Fe_{1/3}Mn_{1/3}]O_2$ Cathodes for Na-Ion Battery Application. *Electrochem. Commun.* **2012**, *18*, 66−69.
(7) Lee, H.; Kim, Y.-I.; Park, J.-K.; Choi, J. W. Sodium Zinc Hexacyanoferrate with a Well-Defined Open Framework as a Positive Electrode for Sodium Ion Batteries. *Chem. Commun.* **2012**, *48*, 8416−8418.
(8) Lim, S. Y.; Kim, H.; Shakoor, R. A.; Jung, Y.; Choi, J. W. Electrochemical and Thermal Properties of NASICON Structured $Na_3V_2(PO_4)_3$ as a Sodium Rechargeable Battery Cathode: A Combined Experimental and Theoretical Study. *J. Electrochem. Soc.* **2012**, *159*, A1393−A1397.
(9) Sun, Q.; Ren, Q.-Q.; Fu, Z.-W. NASICON-Type $Fe_2(MoO_4)_3$ Thin Film as Cathode for Rechargeable Sodium Ion Battery. *Electrochem. Commun.* **2012**, *23*, 145−148.
(10) Wessells, C. D.; McDowell, M. T.; Peddada, S. V.; Pasta, M.; Huggins, R. A.; Cui, Y. Tunable Reaction Potentials in Open Framework Nanoparticle Battery Electrodes for Grid-Scale Energy Storage. *ACS Nano* **2012**, *6*, 1688−1694.
(11) Wessells, C. D.; Peddada, S. V.; Huggins, R. A.; Cui, Y. Nickel Hexacyanoferrate Nanoparticle Electrodes For Aqueous Sodium and Potassium Ion Batteries. *Nano Lett.* **2011**, *11*, 5421−5425.
(12) Xia, X.; Dahn, J. R. $NaCrO_2$ is a Fundamentally Safe Positive Electrode Material for Sodium-Ion Batteries with Liquid Electrolytes. *Electrochem. Solid-State Lett.* **2012**, *15*, A1−A4.
(13) Moreau, P.; Guyomard, D.; Gaubicher, J.; Boucher, F. Structure and Stability of Sodium Intercalated Phases in Olivine $FePO_4$. *Chem. Mater.* **2010**, *22*, 4126−4128.
(14) Liu, Y.; Xu, Y.; Han, X.; Pellegrinelli, C.; Zhu, Y.; Zhu, H.; Wan, J.; Chung, A. C.; Vaaland, O.; Wang, C.; et al. Porous Amorphous FePO4 Nanoparticles Connected by Single-Wall Carbon Nanotubes for Sodium Ion Battery Cathodes. *Nano Lett.* **2012**, *12*, 5664−5668.
(15) Chevrier, V. L.; Ceder, G. Challenges for Na-ion Negative Electrodes. *J. Electrochem. Soc.* **2011**, *158*, A1011−A1014.
(16) Alcántara, R.; Jiménez-Mateos, J. M.; Lavela, P.; Tirado, J. L. Carbon Black: a Promising Electrode Material for Sodium-Ion Batteries. *Electrochem. Commun.* **2001**, *3*, 639−642.
(17) Stevens, D. A.; Dahn, J. R. The Mechanisms of Lithium and Sodium Insertion in Carbon Materials. *J. Electrochem. Soc.* **2001**, *148*, A803−A811.
(18) Abel, P. R.; Lin, Y.-M.; Celio, H.; Heller, A.; Mullins, C. B. Improving the Stability of Nanostructured Silicon Thin Film Lithium-Ion Battery Anodes through Their Controlled Oxidation. *ACS Nano* **2012**, *6*, 2506−2516.
(19) Abel, P. R.; Chockla, A. M.; Lin, Y.-M.; Holmberg, V. C.; Harris, J. T.; Korgel, B. A.; Heller, A.; Mullins, C. B. Nanostructured $Si_{(1-x)}Ge_x$ for Tunable Thin Film Lithium-Ion Battery Anodes. *ACS Nano* **2013**, *7*, 2249−2257.
(20) Lin, Y.-M.; Klavetter, K. C.; Abel, P. R.; Davy, N. C.; Snider, J. L.; Heller, A.; Mullins, C. B. High Performance Silicon Nanoparticle Anode in Fluoroethylene Carbonate-Based Electrolyte for Li-Ion Batteries. *Chem. Commun.* **2012**, *48*, 7268−7270.
(21) Klavetter, K. C.; Wood, S. M.; Lin, Y.-M.; Snider, J. L.; Davy, N. C.; Chockla, A. M.; Romanovicz, D. K.; Korgel, B. A.; Lee, J.-W.; Heller, A.; et al. A High-Rate Germanium-Particle Slurry Cast Li-Ion Anode with High Coulombic Efficiency and Long Cycle Life. *J. Power Sources* **2013**, *238*, 123−136.
(22) Chockla, A. M.; Klavetter, K. C.; Mullins, C. B.; Korgel, B. A. Solution-Grown Germanium Nanowire Anodes for Lithium-Ion Batteries. *ACS Appl. Mater. Interfaces* **2012**, *4*, 4658−4664.
(23) Beattie, S. D.; Larcher, D.; Morcrette, M.; Simon, B.; Tarascon, J.-M. Si Electrodes for Li-Ion Batteries—A New Way to Look at an Old Problem. *J. Electrochem. Soc.* **2008**, *155*, A158−A163.
(24) Dimov, N.; Kugino, S.; Yoshio, M. Carbon-Coated Silicon as Anode Material for Lithium Ion Batteries: Advantages and Limitations. *Electrochim. Acta* **2003**, *48*, 1579−1587.
(25) Maranchi, J. P.; Hepp, A. F.; Kumta, P. N. High Capacity, Reversible Silicon Thin-Film Anodes for Lithium-Ion Batteries. *Electrochem. Solid-State Lett.* **2003**, *6*, A198−A201.
(26) Chan, C. K.; Peng, H.; Liu, G.; McIlwrath, K.; Zhang, X. F.; Huggins, R. A.; Cui, Y. High-Performance Lithium Battery Anodes Using Silicon Nanowires. *Nat. Nanotechnol.* **2008**, *3*, 31−35.
(27) Seo, M.-H.; Park, M.; Lee, K. T.; Kim, K.; Kim, J.; Cho, J. High Performance Ge Nanowire Anode Sheathed with Carbon for Lithium Rechargeable Batteries. *Energy Environ. Sci.* **2011**, *4*, 425−428.
(28) Liang, W.; Yang, H.; Fan, F.; Liu, Y.; Liu, X. H.; Huang, J. Y.; Zhu, T.; Zhang, S. Tough Germanium Nanoparticles under Electrochemical Cycling. *ACS Nano* **2013**, *7*, 3427−3433.
(29) Baggetto, L.; Notten, P. H. L. Lithium-Ion (De)Insertion Reaction of Germanium Thin-Film Electrodes: An Electrochemical and In Situ XRD Study. *J. Electrochem. Soc.* **2009**, *156*, A169−A175.
(30) Derrien, G.; Hassoun, J.; Panero, S.; Scrosati, B. Nanostructured Sn−C Composite as an Advanced Anode Material in High-Performance Lithium-Ion Batteries. *Adv. Mater.* **2007**, *19*, 2336−2340.
(31) Winter, M.; Besenhard, J. O. Electrochemical Lithiation of Tin and Tin-Based Intermetallics and Composites. *Electrochim. Acta* **1999**, *45*, 31−50.
(32) Courtney, I. A.; McKinnon, W. R.; Dahn, J. R. On the Aggregation of Tin in SnO Composite Glasses Caused by the Reversible Reaction with Lithium. *J. Electrochem. Soc.* **1999**, *146*, 59−68.
(33) Abel, P. R.; Lin, Y.-M.; de Souza, T.; Chou, C.-Y.; Gupta, A.; Goodenough, J. B.; Hwang, G. S.; Heller, A.; Mullins, C. B. Nanocolumnar Germanium Thin Films as a High-Rate Sodium-Ion Battery Anode Material. *J. Phys. Chem. C* **2013**, *117*, 18885−18890.
(34) Baggetto, L.; Keum, J. K.; Browning, J. F.; Veith, G. M. Germanium as Negative Electrode Material for Sodium-Ion Batteries. *Electrochem. Commun.* **2013**, *34*, 41−44.
(35) Ellis, L. D.; Hatchard, T. D.; Obrovac, M. N. Reversible Insertion of Sodium in Tin. *J. Electrochem. Soc.* **2012**, *159*, A1801−A1805.
(36) Datta, M. K.; Epur, R.; Saha, P.; Kadakia, K.; Park, S. K.; Kumta, P. N. Tin and Graphite Based Nanocomposites: Potential Anode for Sodium Ion Batteries. *J. Power Sources* **2013**, *225*, 316−322.
(37) Yamamoto, T.; Nohira, T.; Hagiwara, R.; Fukunaga, A.; Sakai, S.; Nitta, K.; Inazawa, S. Charge−Discharge Behavior of Tin Negative Electrode for a Sodium Secondary Battery Using Intermediate Temperature Ionic Liquid Sodium Bis(Fluorosulfonyl)Amide−Potassium Bis(Fluorosulfonyl)Amide. *J. Power Sources* **2012**, *217*, 479−484.
(38) Baggetto, L.; Ganesh, P.; Meisner, R. P.; Unocic, R. R.; Jumas, J.-C.; Bridges, C. A.; Veith, G. M. Characterization of Sodium Ion Electrochemical Reaction with Tin Anodes: Experiment and Theory. *J. Power Sources* **2013**, *234*, 48−59.
(39) Jow, T. R.; Shacklette, L. W.; Maxfield, M.; Vernick, D. The Role of Conductive Polymers in Alkali-Metal Secondary Electrodes. *J. Electrochem. Soc.* **1987**, *134*, 1730−1733.
(40) Li, H.; Shi, L.; Lu, W.; Huang, X.; Chen, L. Studies on Capacity Loss and Capacity Fading of Nanosized SnSb Alloy Anode for Li-Ion Batteries. *J. Electrochem. Soc.* **2001**, *148*, A915−A922.
(41) Kim, C.; Noh, M.; Choi, M.; Cho, J.; Park, B. Critical Size of a Nano SnO2 Electrode for Li-Secondary Battery. *Chem. Mater.* **2005**, *17*, 3297−3301.
(42) Komaba, S.; Matsuura, Y.; Ishikawa, T.; Yabuuchi, N.; Murata, W.; Kuze, S. Redox Reaction of Sn-Polyacrylate Electrodes in Aprotic Na Cell. *Electrochem. Commun.* **2012**, *21*, 65−68.
(43) Beattie, S. D.; Hatchard, T.; Bonakdarpour, A.; Hewitt, K. C.; Dahn, J. R. Anomalous, High-Voltage Irreversible Capacity in Tin Electrodes for Lithium Batteries. *J. Electrochem. Soc.* **2003**, *150*, A701−A705.
(44) Gu, M.; Kushima, A.; Shao, Y.; Zhang, J.-G.; Liu, J.; Browning, N. D.; Li, J.; Wang, C. Probing the Failure Mechanism of SnO2 Nanowires for Sodium-Ion Batteries. *Nano Lett.* **2013**, *13*, 5203−5211.
(45) Wang, Y.-X.; Lim, Y.-G.; Park, M.-S.; Chou, S.-L.; Kim, J. H.; Liu, H.-K.; Dou, S.-X.; Kim, Y.-J. Ultrafine SnO2 Nanoparticle Loading onto Reduced Graphene Oxide as Anodes for Sodium-Ion Batteries

with Superior Rate and Cycling Performances. *J. Mater. Chem. A* **2014**, *2*, 529−534.
(46) Wu, L.; Hu, X.; Qian, J.; Pei, F.; Wu, F.; Mao, R.; Ai, X.; Yang, H.; Cao, Y. A Sn-SnS-C Nanocomposite as Anode Host Materials for Na-Ion Batteries. *J. Mater. Chem. A* **2013**, *1*, 7181−7184.
(47) Xu, Y.; Zhu, Y.; Liu, Y.; Wang, C. Electrochemical Performance of Porous Carbon/Tin Composite Anodes for Sodium-Ion and Lithium-Ion Batteries. *Adv. Energy Mater.* **2013**, *3*, 128−133.
(48) Lin, Y.-M.; Abel, P. R.; Gupta, A.; Goodenough, J. B.; Heller, A.; Mullins, C. B. Sn−Cu Nanocomposite Anodes for Rechargeable Sodium-Ion Batteries. *ACS Appl. Mater. Interfaces* **2013**, *5*, 8273−8277.
(49) Thorne, J. S.; Dunlap, R. A.; Obrovac, M. N. $Cu6Sn5)_{1-x}C_x$ Active/Inactive Nanocomposite Negative Electrodes for Na-Ion Batteries. *Electrochim. Acta* **2013**, *112*, 133−137.
(50) Olesinski, R. W.; Abbaschian, G. J. The Ge−Sn (Germanium−Tin) system. *Bull. Alloy Phase Diagrams* **1984**, *5*, 265−271.
(51) Temkin, R. J.; Connell, G. A. N.; Paul, W. Structural and Optical Properties of Amorphous Ge_xSn_{1-x} Alloys. *Solid State Commun.* **1972**, *11*, 1591−1595.
(52) Tamura, K.; Fukushima, J.; Endo, H.; Minomura, S.; Shimomura, O.; Asaumi, K. Non-Metal to Metal Transition in Amorphous Ge and Ge-Sn Alloys under High Pressure. *J. Phys. Soc. Jpn.* **1974**, *36*, 558−564.
(53) Bodnarchuk, M. I.; Kravchyk, K. V.; Krumeich, F.; Wang, S.; Kovalenko, M. V. Colloidal Tin−Germanium Nanorods and Their Li-Ion Storage Properties. *ACS Nano* **2014**, *8*, 2360−2368.
(54) Fan, S.; Lim, L. Y.; Tay, Y. Y.; Pramana, S. S.; Rui, X.; Samani, M. K.; Yan, Q.; Tay, B. K.; Toney, M. F.; Hng, H. H. Rapid Fabrication of a Novel Sn-Ge Alloy: Structure-Property Relationship and its Enhanced Lithium Storage Properties. *J. Mater. Chem. A* **2013**, *1*, 14577−14585.
(55) Cho, Y. J.; Kim, C. H.; Im, H. S.; Myung, Y.; Kim, H. S.; Back, S. H.; Lim, Y. R.; Jung, C. S.; Jang, D. M.; Park, J.; et al. Germanium-Tin Alloy Nanocrystals for High-Performance Lithium Ion Batteries. *Phys. Chem. Chem. Phys.* **2013**, *15*, 11691−11695.
(56) Farbod, B.; Cui, K.; Kalisvaart, W. P.; Kupsta, M.; Zahiri, B.; Kohandehghan, A.; Lotfabad, E. M.; Li, Z.; Luber, E. J.; Mitlin, D. Anodes for Sodium Ion Batteries Based on Tin−Germanium−Antimony Alloys. *ACS Nano* **2014**, *8*, 4415−4429.
(57) Robbie, K.; Sit, J. C.; Brett, M. J. Advanced Techniques for Glancing Angle Deposition. *J. Vac. Sci. Technol., B* **1998**, *16*, 1115−1122.
(58) Abelmann, L.; Lodder, C. Oblique Evaporation and Surface Diffusion. *Thin Solid Films* **1997**, *305*, 1−21.
(59) Krause, K. M.; Thommes, M.; Brett, M. J. Pore Analysis of Obliquely Deposited Nanostructures by Krypton Gas Adsorption at 87 K. *Microporous Mesoporous Mater.* **2011**, *143*, 166−173.
(60) Hawkeye, M. M.; Brett, M. J. Glancing Angle Deposition: Fabrication, Properties, and Applications of Micro- and Nanostructured Thin Films. *J. Vac. Sci. Technol., A* **2007**, *25*, 1317−1335.
(61) Lin, Y.-M.; Abel, P. R.; Flaherty, D. W.; Wu, J.; Stevenson, K. J.; Heller, A.; Mullins, C. B. Morphology Dependence of the Lithium Storage Capability and Rate Performance of Amorphous TiO_2 Electrodes. *J. Phys. Chem. C* **2011**, *115*, 2585−2591.
(62) Flaherty, D. W.; Hahn, N. T.; May, R. A.; Berglund, S. P.; Lin, Y.-M.; Stevenson, K. J.; Dohnalek, Z.; Kay, B. D.; Mullins, C. B. Reactive Ballistic Deposition of Nanostructured Model Materials for Electrochemical Energy Conversion and Storage. *Acc. Chem. Res.* **2012**, *45*, 434−443.
(63) Maruyama, T.; Akagi, H. Thin Films of Amorphous Germanium-Tin Alloys Prepared by Radio-Frequency Magnetron Sputtering. *J. Electrochem. Soc.* **1998**, *145*, 1303−1305.
(64) Bauer, M. R.; Tolle, J.; Bungay, C.; Chizmeshya, A. V. G.; Smith, D. J.; Menéndez, J.; Kouvetakis, J. Tunable Band Structure in Diamond−Cubic Tin−Germanium Alloys Grown on Silicon Substrates. *Solid State Commun.* **2003**, *127*, 355−359.
(65) He, G.; Atwater, H. A. Synthesis of Epitaxial Sn_xGe_{1-x} Alloy Films by Ion-Assisted Molecular Beam Epitaxy. *Nucl. Instrum. Methods Phys. Res., Sect. B* **1995**, *106*, 126−132.
(66) Abel, P. R.; Lin, Y.-M.; de Souza, T.; Chou, C.-Y.; Gupta, A.; Goodenough, J. B.; Hwang, G. S.; Heller, A.; Mullins, C. B. Nanocolumnar Germanium Thin Films as a High-Rate Sodium-Ion Battery Anode Material. *J. Phys. Chem. C* **2013**, *117*, 18885−18890.
(67) Kolodzey, J.; Coppinger, M.; Kim, S.; Bhargava, N.; Gupta, J.; Chaoying, N.; Yung Kee, Y. In *The Properties of Germanium-Tin Alloys for Infrared Device Applications*, Semiconductor Device Research Symposium (ISDRS), 2011 International, 7−9 Dec. 2011; pp 1−1.
(68) Hall, L. A. *Survey of Electrical Resistivity Measurements on 16 Pure Metals in the Temperature Range 0 to 273 K*; U.S. Dept. of Commerce, National Bureau of Standards: Washington, D.C., 1968; p 111.
(69) Ewald, A. W.; Tufte, O. N. Electronic Properties of Gray Tin Single Crystals. *J. Phys. Chem. Solids* **1959**, *8*, 523−525.
(70) Sharma, S. K.; Jain, S. C.; Aggarwal, S. S.; Bhide, V. G. Structure and Electrical Resistivity of Thin Amorphous Germanium Films. *J. Non-Cryst. Solids* **1972**, *7*, 285−294.